

Chapter 2

Introduction to Discrete Element Method

This chapter provides a review of the theories and methodologies of the Discrete Element Method (DEM), and its validation via numerical triaxial tests on sands. Based on the triaxial tests and granular column collapse model, the fundamental strength properties of material internal friction angle and stress–strain behaviour have been studied. The goal of this study is to calibrate these parameters, so that they can be used in the investigation of the mechanical behaviour of granular flows will be presented in the following chapters.

2.1 The Discrete Element Method

The Discrete Element Method (DEM) is a numerical method for modelling the dynamics of solid particles which interact with each other at discrete contact points. Since it was firstly proposed by Cundall and Strack (1979) to study the mechanical behaviour of rock at the microscopic level, the DEM has been developed rapidly, with applications in rock/soil mechanics, chemical engineering and pharmacy (Thornton 2000; Cleary and Sawley 2002; Cui and O’Sullivan 2006; Wu and Cocks 2006; Jing and Stephansson 2007; Lu and McDowell 2007; Ng 2009; Plassiard et al. 2009; Yu et al. 2013).

In DEM simulations, the properties of a stressed assembly of rigid spherical particles (e.g. position, velocity and contact forces) are updated at every numerical iteration time step. The translational and rotational displacements of each particle are obtained by explicitly integrating the governing differential equations based on the Newton’s second law of motion, while the contact forces between particles are calculated using well-defined force–displacement contact models (Hertz 1882; Mindlin and Deresiewicz 1953; Cundall and Strack 1979; Itasca 2003). In this process, the interactions between particles are monitored at all contacts and the movement of each individual particle is traced. It is assumed that the velocity of

each particle is constant within each iteration step. Since the explicit integration technique is used in the DEM calculation, the time step is required to be very small so that stable numerical solutions can be achieved.

Figure 2.1 illustrates the mechanical loop of the DEM calculations. The simulation starts by detecting the contact points between particles. The contact point and the particle overlapping distance are then used to calculate the interaction forces via the force–displacement relationships. The resulting contact forces are applied at the centre of each particle, causing particles to move. According to the Newton’s second law of motion, the particle acceleration, velocity and displacement are updated at the end of each numerical iteration step. This mechanical loop continues until the prescribed total iteration steps are reached.

2.1.1 Particle Motion

According to the Newton’s second law of motion, the equation governing the translational motion of a single particle is expressed as

$$m_i \frac{d^2}{dt^2} \vec{x}_i = m_i \vec{g} + \sum_{N_c} (\vec{f}_{nc} + \vec{f}_{tc}) + \vec{f}_{fluid} \quad (2.1)$$

where m_i is the mass of a particle i ; \vec{x}_i is the position of its centroid; \vec{g} is the gravitational acceleration; \vec{f}_{nc} and \vec{f}_{tc} are the normal and tangential inter-particle contact forces exerted by the neighbouring particles; the summation of the contact forces are over all the contacts (N_c); \vec{f}_{fluid} is the interaction forces between fluid and particles, as will be discussed in Sect. 4.1.

The rotational motion of a single particle is given as below

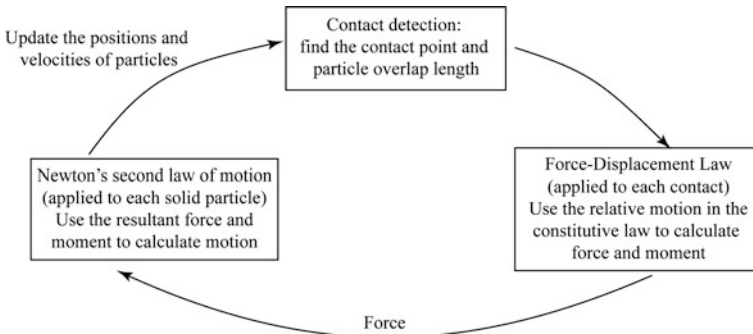


Fig. 2.1 Calculation cycle in the DEM

$$I_i \frac{d}{dt} \vec{\omega}_i = \sum_{Nc} \vec{r}_c \times \vec{f}_{ic} + \vec{M}_r, \quad (2.2)$$

where I_i is the moment of inertia about the grain centroid; $\vec{\omega}_i$ is the angular velocity; \vec{r}_c is the vector from the particle mass centre to the contact point; \vec{M}_r is the rolling resistant moment, which inhibits particle rotation over other particles.

2.1.2 The Particle—Particle Contact Model

The accuracy of DEM modelling depends highly on the contact models used to calculate the particle–particle interactions. This topic has long been discussed by geotechnical researchers, such as Iwashita (1998), Jiang et al. (2005) and Belheine et al. (2009). The fundamental problem is how to reproduce the correct interactions between two solid grains in the DEM. The classical DEM model treats all solid grains as either disks (i.e. two-dimensional (2D) model) or spheres (i.e. three-dimensional (3D) model), as this would greatly simplify the calculation of the overlap distance between particles. Though this model has shed some lights on the mechanical behaviour of granular materials, it is inaccurate due to the oversimplified assumptions that all solid particles are spherical and free to rotate. However, real particles and their contacts are much more complicated, for example, the particle is normally not spherical and have a rough surface texture, possibly can be covered by a thin film of weathered materials. For non-spherical particles, the line of action of the normal contact force no longer passes through the centre of mass of the particles and hence generating rotational moments (Belheine et al. 2009).

To account for the particle shape effects, three ways of DEM modelling can be used. The first of the three is to use a clump of spherical particles based on the bonded-particle method (Potyondy and Cundall 2004). In this method, the real shape of soil/rock mass is approximated by a clump of bonded spherical grains, which behaves as a rigid body. The second approach is to model the soil/rock blocks as polygons (Cundall 1988; Boon et al. 2012). The third method is to include the rolling resistant moment at the particle contacts (Jiang et al. 2005). This research uses the last method in simulating the mechanical behaviour of granular materials due to its simplicity.

As shown in Fig. 2.2, the real solid grains have irregular shapes, while the DEM model approximates the irregular shape with circles (or spheres). Because of this simplification, the contact point detected in the numerical model can be dramatically different from the real one. The distance between the real and numerical contact points is defined as ηr , with r being the average radius between the two particles in contact; η being a coefficient quantifying the offset of the contact point. In addition, the position of the contact point might change during the simulation as individual grains can rotate due to the unbalanced moment acting on the geometrical centre. Assuming particle B rotates in the anticlockwise direction, the resultant

rolling resistant moment from the normal contact force would act in the clockwise direction, resisting the particle rotation. For simplicity, the rolling resistant moment is defined to act in a direction opposite to the relative rotation.

The open source DEM code ESyS-Particle (Weatherley et al. 2011) was employed to run simulations presented herein. Using this code, a series of preliminary runs of granular column collapse tests (see Chap. 3) employing the non-linear, elastic Hertz–Mindlin contact model (Hertz 1882; Mindlin and Deresiewicz 1953) and linear elastic contact model (Zhang and Whiten 1996) have been conducted. No significant difference was found. Hence, since the linear elastic contact requires less computational time, it is used in the current research. The detailed description of the model can be found in Jiang et al. (2005) and Belheine et al. (2009). As shown in Fig. 2.3, the classical DEM model may be modified by introducing an additional rolling moment component at each contact point whereby rolling resistance can be accounted for. Thus, three distinct particle contact models can be identified, namely, (a) the normal contact model; (b) the tangential contact model; and (c) the rolling contact model. The mechanical responses of these three different contact models are closely related to the relative displacement between the two particles, as shown in Fig. 2.4. The interaction forces between two spheres include the normal (F_n) and tangential (F_t) forces, and rolling moment (M_r), respectively.

In Fig. 2.4a, the normal contact force (F_n) acting on a single particle is linearly proportional to the overlap distance between two particles, which is expressed as

$$F_n = K_n \cdot U_n \quad (2.3)$$

in which K_n is the normal contact stiffness, U_n is the normal overlap distance.

Figure 2.4b shows that a maximum tangential force ($F_n \tan(\theta)$) exists, before which, the tangential force (F_t) can be calculated incrementally, as

Fig. 2.2 The approximation of real grain contact using the DEM model

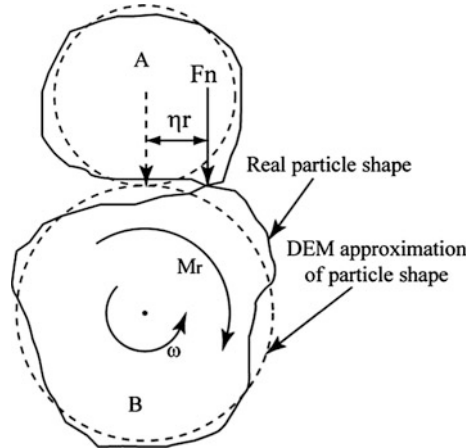


Fig. 2.3 The contact model between two spheres (cited from Jiang et al. (2005), p. 348)

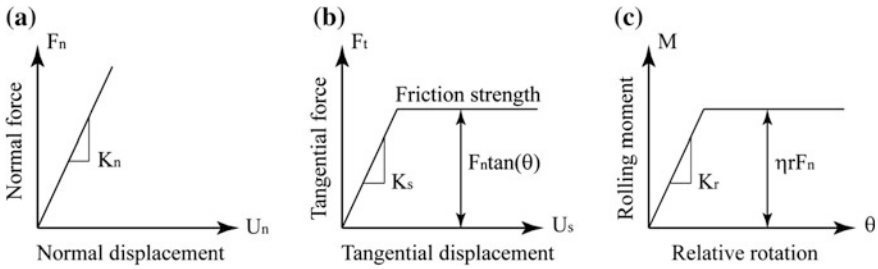
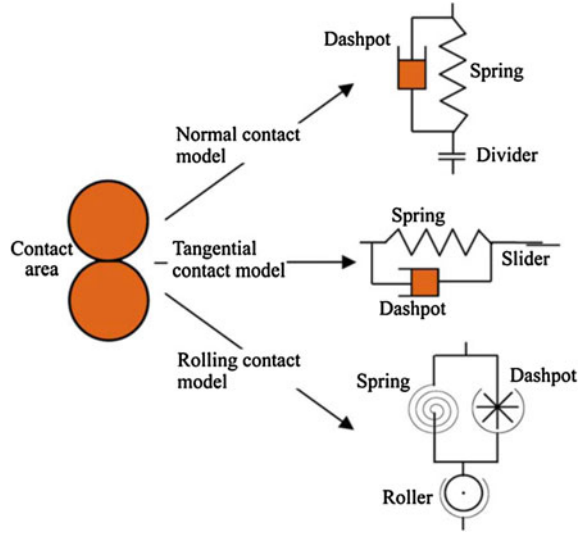


Fig. 2.4 Particle contact model (cited from Belheine et al. (2009), p. 324)

$$F_t^n = F_t^{n-1} + K_s \cdot dU_s, \quad (2.4)$$

where F_t^n and F_t^{n-1} are tangential forces calculated at current and previous iteration steps. K_s is the shear stiffness, and dU_s is the incremental tangential sliding displacement.

Figure 2.4c shows that the rolling resistant moment increases gradually from zero to the maximum value when two particles come into contact and rotate over each other. The magnitude of elastic rolling moment (M_r) is proportional to the relative rotational angle, as calculated incrementally by Eq. (2.5).

$$M_r^n = M_r^{n-1} + K_r \cdot \Delta\theta_r, \quad (2.5)$$

where M_r^n and M_r^{n-1} are the rolling moment calculated at the current and previous iteration steps; $K_r = \beta K_s r^2$ is the rolling stiffness, with β being the coefficient of

rolling stiffness, r being the average particle radius at contact (i.e. $r = (R_1 + R_2)/2$); $\Delta\theta_r$ is the relative rotational angle between the two particles within one iteration time step. The magnitude of the maximum rolling moment is defined as

$$M_p = \eta \cdot r \cdot |F_n| \quad (2.6)$$

in which, η is the coefficient of plastic moment.

2.1.3 The Calculation of Stress in the DEM

As the DEM is applicable only for modelling the mechanical behaviour of discrete materials (e.g. sand and rock), it is not straightforward to obtain the stress distribution within the granular assembly based on the definition of stress in continuum mechanics. Instead, in the DEM, the homogenization or micro-macro averaging technique is used to calculate the stress tensor (Thornton and Antony 2000). For an assembly of granular materials within a measurement volume (V), the stress tensor ($\bar{\sigma}_{ij}$) is defined as

$$\bar{\sigma}_{ij} = - \left(\frac{1-n}{\sum_{N_p} V^{(p)}} \right) \sum_{N_p} \sum_{N_c} \left| x_i^{(c)} - x_i^{(p)} \right| n_i^{(c,p)} F_j^{(c)} \quad (2.7)$$

where the summation is taken over N_p particles with their centroids locating within the measurement volume; n is the porosity of the measurement volume; $V^{(p)}$ is the volume of a single particle; N_c is the number of contacts around a single particle; $x_i^{(p)}$ is the location of the particle centroid, and $n_i^{(c,p)}$ is the unit normal directed from the particle centre to the contact location ($x_i^{(c)}$); $F_j^{(c)}$ is the force acting at the contact.

2.1.4 Coordination Number

The concept of coordination number comes from chemistry and crystallography, where it is defined as the number of atoms around a central atom in a molecule or crystal (De 2007; Hermann et al. 2007). In the DEM, this variable is used to quantify the packing state of granular materials. The coordination number of a particle is the number of neighbouring particles it contacts with. As studied in the numerical biaxial tests (Thornton 2000; Jiang et al. 2010), the coordination number has been identified as an important variable to study soil failure. According to Jiang et al. (2010), the coordination number is small in the shear band of soil sample. By tracking the distribution of coordination number, it is possible to identify the

potential weak zone of soil sample. During the simulation, the bulk coordination number of a granular assembly in a volume (V) is calculated via the coordination number of individual particles (C_i), as

$$\bar{C} = \frac{1}{N_p} \sum_{i=1}^{N_p} C_i, \quad (2.8)$$

where N_p is the total number of particles within the volume.

2.2 Model Validation

The previously discussed DEM model was validated by performing numerical triaxial tests on sands. The properties of the sand sample are selected by trial and error, close to those reported in the literature, and will be used in the analyses of the next chapters.

2.2.1 Input Parameters of the DEM Model

The particle-size distribution (PSD) is one of the most important material properties controlling soil strength, deformation and permeability. The PSD of debris flows vary hugely at different locations (see for instance Casagli et al. 2003). In addition, the grain-size distribution may vary significantly within the same landslide mass at different depths (Crosta et al. 2007). Figure 2.5 shows examples of particle-size distributions from seven landslide sites in the Northern Apennines (Casagli et al. 2003) and six cases of rock avalanches in Val Pola in the Alps (Crosta et al. 2007). It can be observed that the grain size ranges from 0.001 to 1000 mm, with a large percentage of fine- and medium-sized grains and a small amount of coarse grains. Large discrepancies can be observed between the various site investigations.

According to Fig. 2.5, the solid grains with diameters ranging from 0.1 to 10 mm were widely observed in different locations. However, in DEM simulations, due to computational limitations, a much narrower particle-size distribution with the ratio of maximum to minimum particle sizes of 2 is used, as shown by the red curve in Fig. 2.5. The input parameters are listed in Table 2.1.

2.2.2 Determination of Numerical Time Step

The choice of the numerical time step used in the DEM simulation is very important because if it is too large, inaccurate results and violation of thermodynamic laws

Fig. 2.5 Particle size distribution of landslides in the Northern Apennines (Italy) (after Casagli et al. 2003) and rock avalanches in the Alps (Italy) (after Crosta et al. 2007). The particle size distribution adopted in the numerical simulations is plotted as the dashed *red curve*

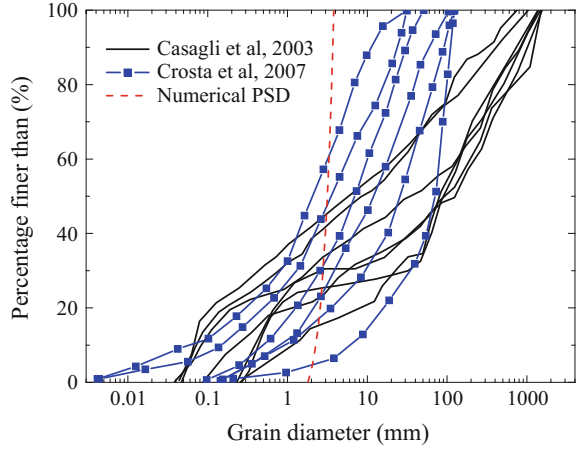


Table 2.1 Input parameters of DEM simulations

DEM parameters	Value	DEM parameters	Value
Particle diameter, D (mm)	See Fig. 2.5	Damping coefficient	0.0
Sample packing porosity, n	(Loose) 0.45 (Dense) 0.37	Coefficient of rolling stiffness, β	1.0
Particle density, ρ_s (kg/m ³)	2650	Coefficient of plastic moment, η	0.1
Normal stiffness, K_n (N/m)	3×10^7	<i>Simulation parameters</i>	<i>Value</i>
Shear stiffness, K_s (N/m)	2.7×10^7	Gravity, g (m/s ²)	-9.81
Particle friction angle, θ (°)	30	DEM Time step, Δt (s)	10^{-7}

(i.e. violation of conservation of energy) may result (Tsuji et al. 1993). Since the linear elasticity contact model is adopted in the current simulations, the time step is assumed to have a simple expression (Bathe and Wilson 1976; Tsuji et al. 1992) of

$$\Delta t = \lambda \sqrt{m/K_n}, \quad (2.9)$$

where λ is a reduction factor; m is the particle mass; K_n is the normal contact stiffness.

Theoretically, a system consisting of a large number of particles should conserve energy if no energy dissipation mechanism is active. However, the explicit numerical integration techniques (e.g. forward, backward or central difference) used in the DEM, would inevitably lead to slight numerical errors in the calculations of grain velocity and position during each iteration step. These numerical errors result from the assumption adopted in the DEM that the velocities of solid grains can keep constant within one iteration time step. However, it is not true for the real granular system, because the forces acting on solid grains might vary over time. In general, the larger the numerical time step employed in the simulations, the larger the resulting errors introduced in the analyses. Thus, to conserve energy in numerical

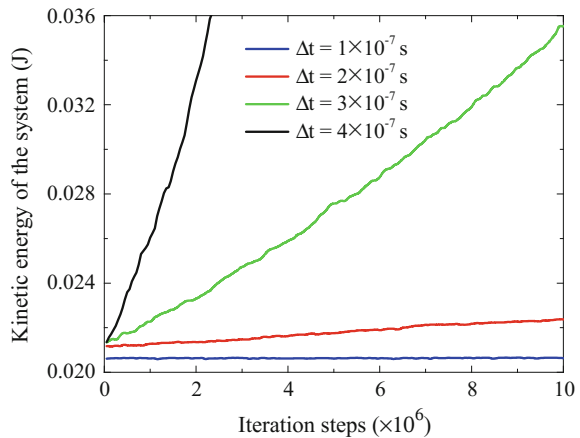
simulations, a proper reduction factor (λ), should be used in Eq. (2.9) to obtain a smaller numerical time step, such that the integration errors can be neglected.

Hence, in this work, to determine the time step, simulations of elastic particle collision using various values of time step have been performed, in which 1250 particles were randomly generated within a prismatic box. The initial velocities of these particles were randomly set with each component in a range of $[-1.0, 1.0]$ m/s employing the Mersenne Twister algorithm (Matsumoto and Nishimura 1998). All particle collisions, either particle–particle or particle–wall collision, are purely elastic (i.e. the coefficient of restitution is equal to 1.0). In addition, the gravity, friction coefficient, rolling and damping parameters were all set to zero, so that no mechanism of energy dissipation exists. Other DEM parameters have the same values as those listed in Table 2.1.

In Fig. 2.6, the results are plotted in terms of kinetic energy of the granular system against time. It emerges that for time step larger than 1.0×10^{-7} s, the total kinetic energy of the granular system is not conserved even though no mechanism of energy dissipation is introduced in the tests. The lack of energy conservation can be entirely ascribed to the numerical algorithm of the DEM code. Further decrease of time step would significantly increase the computational cost. Thus, the value 1.0×10^{-7} s is chosen as the proper time step used in this research. This issue with DEM simulations has been discussed by Tsuji et al. (1992). Unfortunately there are several publications where no parametric analysis on the choice of the time step is carried out, so that the simulations may be affected by errors due to the unphysical artificial energy introduced by the numerical algorithms employed.

According to the discussion above, the elastic grain collision model has effectively determined the time step of an un-damped granular system. As the un-damped particles can move faster than grains in a damped condition (e.g. models with granular friction, fluid viscous drag forces and plastic contacts) under the same initial and boundary conditions, the time step determined by the current model would be smaller than the theoretical time step used in the granular flow model.

Fig. 2.6 The kinetic energy of the granular system



Thus, the time step determined in this section can be used in the subsequent simulations of granular flows and submerged debris flows.

In the DEM–CFD model, the DEM time step is determined by the elastic grain collision model, while the maximum time step used in the CFD is determined by the Courant–Friedrichs–Lewy condition (CFL condition) (Courant 1928; Guo 2010) that the Courant number of the system should be smaller than 1.0.

$$C = \frac{nU_r \cdot \Delta t}{\Delta x} \leq 1.0, \quad (2.10)$$

where C is the Courant number; U_r is the relative velocity between fluid and solid particle; Δx is the minimum size of a CFD mesh cell; Δt is the time step used in the CFD.

According to Eq. (2.10), the time step used in the CFD should satisfy the condition as

$$\Delta t \leq \frac{\Delta x}{nU_r} \quad (2.11)$$

According to Eqs. (2.9) and (2.11), the critical time step used in the CFD model is generally larger than that used in the DEM simulation (Kafui et al. 2002). Therefore, in numerical simulations using the DEM–CFD coupling method, the total numerical simulation time is mainly determined by the critical time step of the DEM model.

In this research, no numerical damping was employed. There are two reasons to be considered. First, although several damping models exist in the literature, few of them have physical bases. The use of damping can dissipate kinetic energy in a granular system and bring the whole system to the steady state very quickly. As a result, it is often used in quasi-static simulations as only the static state is of interest (Jiang et al. 2005; Modenese et al. 2012). However, in the simulations of landslides, the granular materials would go through dynamic motion, such that any damping would alter the mechanical behaviour of the system significantly. Even though the viscous damping forces have been used to model energy dissipation due to plastic particle contacts (Brilliantov et al. 2007), the magnitude of energy dissipation is very difficult to be evaluated correctly. Thus, this research assumes that the energy dissipation in landslides only comes from frictions between particles.

2.2.3 Numerical Simulation of Triaxial Tests

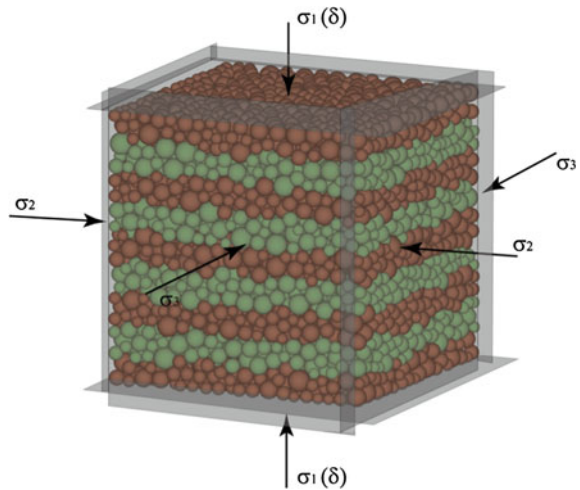
Both the strength and stiffness of soil can influence the mechanical behaviour of landslides at different stages of granular motion. For instance, the elastic deformation under loading is mainly determined by the stiffness properties (e.g. Young's Modulus), while for slope failure with large deformations, the strength parameters,

such as the peak and residual soil strengths, are dominant (Fang 1991). In this study, the primary purpose is to investigate the large deformation of soil. Thus, the strength parameters are calibrated in this section, so that they can be used to simulate soil behaviour during granular flows. In general, the motion of granular materials is resisted by the sliding friction and geometrical interference (Rowe 1962; Terzaghi et al. 1996), when grains slide along the adjacent particle surfaces. This frictional effect is characterized by the internal friction angle of granular materials (φ) which depends mainly on the particle surface roughness and interlocking, while it is independent of the confining stress and density (Barrett 1980). As the drained strength of sand is widely used in experimental and numerical studies, the current research will mainly focus on the calibration of soil strength properties using the numerical drained triaxial tests. Particular emphasis is given to the soil behaviour at the critical state, i.e. the state that soil mass can be sheared continuously without further changes in stresses and volume (Schofield and Wroth 1968; Wood 1990).

2.2.3.1 Model Configuration

The DEM triaxial testing model for drained condition of sands is shown in Fig. 2.7. An assembly of polydispersed solid grains is packed within a parallelepiped prism bounded by six smooth and rigid walls. These walls can move freely so that the prescribed confining stress and strain can be achieved. The particle properties, such as particle-size distribution, contact stiffness are listed in Table 2.1. Since the quasi-static (QS) conditions are desired during the triaxial tests, the particle density is scaled up to be $2.65 \times 10^{12} \text{ kg/m}^3$. In such a case, the inertial forces of grains are

Fig. 2.7 The DEM model configuration of the triaxial test



negligible when compared with the inter-particle contact forces (Thornton and Antony 1998; Modenese 2013).

The triaxial test consists of two stages: isotropic compression and deviatoric shear. In the isotropic compression stage, the same confining pressures are applied on the boundary walls in the x -, y - and z -directions. The magnitude of the confining pressure increases gradually from zero to the projected confining pressure (p_0). After reaching p_0 , the confining pressures will remain constant until the deviatoric shear stage starts. In the deviatoric shear stage, the confining pressures in the lateral directions are maintained constant (i.e. $\sigma_2 = \sigma_3 = p_0$), while the sample is compressed in the vertical direction at a constant strain rate (e.g. 10^{-4} s^{-1}). The deviatoric shear of the soil sample continues until the prescribed axial strain is reached (e.g. 30%).

Loose and dense granular samples are obtained using different inter-particle friction and rolling parameters. For loose samples, the friction and rolling coefficients are set as the same values as those listed in Table 2.1, and the isotropic compression can produce a relatively loose granular sample. Dense samples are prepared as the following steps:

- (i) Isotropic compression of the sample with zero friction and rolling coefficients until the aimed confining pressure and QS conditions are reached;
- (ii) Set the inter-particle friction and rolling coefficients to those listed in Table 2.1 and a sufficient number of iteration steps are used to stabilize the sample;
- (iii) Isotropic compression of the sample until the desired confining pressure and QS conditions are reached.

The total number of particles in the model is 10,000, which can satisfy the definition of Representative Elementary Volume (REV) of triaxial tests (Modenese 2013). By using the REV, the number of particles in the model is believed to be large enough, such that the size of the DEM sample has no impact on the numerical results. After sample generation, the dense and loose samples have porosities of 0.37 and 0.45, respectively.

2.2.3.2 Results

In the analyses, the compressive components of stress are defined as positive. The mean and deviatoric stresses are defined as

$$p = (\sigma_1 + \sigma_2 + \sigma_3)/3 \quad (2.12)$$

$$q = (\sigma_1 - \sigma_3) \quad (2.13)$$

These two stress invariants are defined such that, for isotropic, homogeneous materials, p corresponds to the hydrostatic stress, responsible for the isotropic volumetric changes, and q incorporates all the shear stresses which cause the

material distortion. The strain is defined as $\varepsilon_i = -(l_i - L_i)/L_i$, where l_i is the current length of the sample in the i -th direction (e.g. $i = 1$ is for the vertical direction; 2 and 3 are for lateral directions.). L_i is the length of sample prior to deformation. In this definition, the compressive strains are positive, as in classical soil mechanics. The volumetric strain is defined as $\varepsilon_v = -\Delta V/V_0$ with V_0 being the volume prior to the deformation and ΔV being the change of volume.

Figure 2.8 compares the stress–strain and porosity–strain behaviour of the dense and loose sand samples under confining pressures of 50 and 100 kPa, respectively. For the dense sand sample, there is a considerable degree of particle interlocking which, together with the material friction and rolling resistance at contacts, leads to very high shear strength. Thus, the shear stress increases to its peak value at a relatively low strain, and then decreases with the increasing strain as the particle interlocking is progressively overcome. Eventually, the shear stress reaches an ultimate value (i.e. the critical state shear strength at failure). For the loose sand sample, the shear stress increases gradually with the axial strain, until the final peak strength is reached. With the same initial model configurations (e.g. confining pressure, microscopic particle friction and rolling properties), the dense and loose samples will arrive at the same value of critical shear strength.

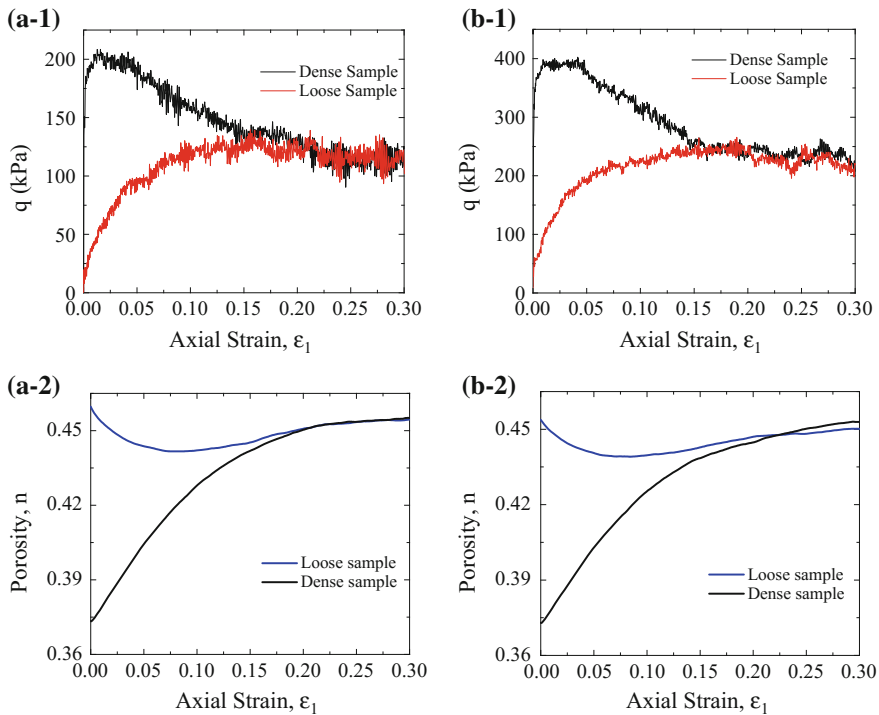


Fig. 2.8 Stress–strain and porosity–strain behaviour: **a** left the lateral confining pressure is 50 kPa and **b** right the lateral confining pressure is 100 kPa

During the deviatoric shear stage, it can be observed that the evolution of porosity of the granular samples at different confining pressures behaves similarly. The loose samples contract, while the dense samples dilate to reach a constant porosity (i.e. 0.454). The axial strain at constant porosity is around 0.20, which corresponds to the axial strain at the critical state. Therefore, the critical state is also called the constant volume state. For simulations at a confining pressure of 100 kPa, the porosity of dense sample is slightly larger than that of loose sample at the critical state. The reason for the observed deviation is due to the large constraints on the rearrangement of solid grains at relatively high confining stresses. The Mohr circles representing stress states at failure are shown in Fig. 2.9a, b, from which the peak and critical (constant volume) material internal friction angle is measured as 41.8° and 32.6° , respectively.

Figure 2.10 illustrates the stress path of loose and dense sand samples during the deviatoric shear stage. In this analysis, triaxial tests using confining pressures of 10, 50 and 100 kPa have been investigated. According to Fig. 2.10a, the deviatoric stress of loose sample increases gradually from zero to the critical shear stress at the failure state. The envelope or the critical state line of the shear strength of sand at failure is a straight line. For the dense sand sample (Fig. 2.10b), the shear stress initially increases to the peak strength in a short period of time. Then, it decreases gradually to reach the critical shear strength at failure.

Based on the discussion above, it can be concluded that the microscopic inter-particle friction angle and rolling parameters can influence the mechanical and deformational behaviour of granular assembly significantly. In order to obtain a comprehensive understanding of how the material internal friction angle is determined by the combination of θ and η , a series of triaxial tests have been conducted. The numerical results obtained are plotted as contour curves in Fig. 2.11. According to Fig. 2.11a, b, it can be observed that the peak material internal friction angle (φ_{peak}) is within a range of $[32^\circ, 51^\circ]$, while the constant volume material internal friction angle (φ_{cv}) is within a range of $[26^\circ, 40^\circ]$. The typical value of φ_{cv} for real quartz sand is found to range from 32° to 34° . For the combination of large values of η and θ , the gradient of internal friction angle contour curves is relatively

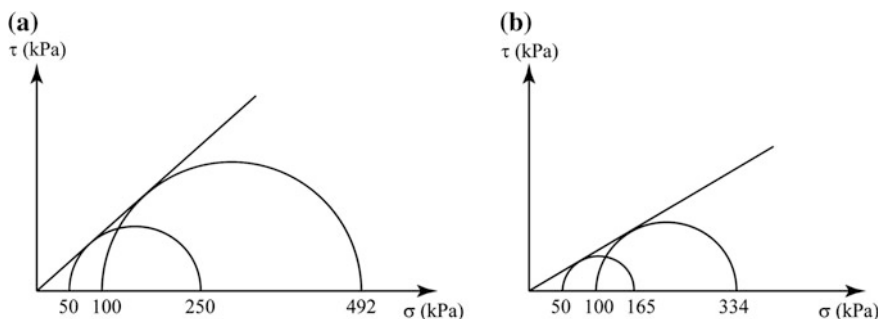


Fig. 2.9 Mohr–Coulomb representation of stress conditions at failure using the maximum and minimum principal stresses: **a** left the peak strength and **b** right the critical strength

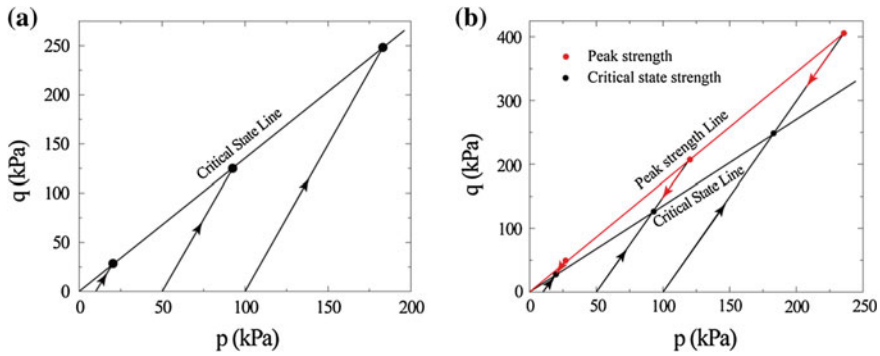


Fig. 2.10 Stress paths for **a** loose sand sample, and **b** dense sand sample

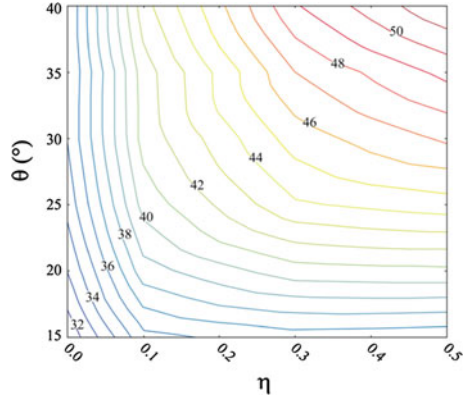
small, indicating that the material internal friction angle is not very sensitive to the change of microscopic particle friction and rolling parameters. From Fig. 2.11c, it can be observed that the higher the inter-particle friction is, the larger the difference between the peak and constant volume material internal friction angles ($\varphi_{\text{peak}} - \varphi_{\text{cv}}$) will be. For typical dense sand materials, the value of ($\varphi_{\text{peak}} - \varphi_{\text{cv}}$) is between 9° and 10° , while for typical loose sand materials, this value is less than 5° .

Based on these graphs, the selection of microscopic particle friction and rolling parameters in the DEM model can be made rationally, so that the projected values of peak and constant volume material internal friction angles can be reproduced. To highlight the influence of θ and η , two series of numerical results of stress–strain and volumetric strain behaviour of the dense DEM samples are illustrated in Fig. 2.12a, b. According to Fig. 2.12a, it can be concluded that on average the inter-particle friction angle can influence the peak strength of soil sample significantly, while little impact is found on the critical state strength. As the inter-particle friction angle ranges from 15° to 40° , the peak shear strength of granular sample increases progressively. However, the critical state strength of soil remains almost unchanged, except for the simulation using an inter-particle friction angle of 15° . High fluctuations of the stress–strain curves is found in simulations using large inter-particle friction angles (i.e. $\theta = 40^\circ$), particularly towards the critical state where particle rearrangement becomes dominant.

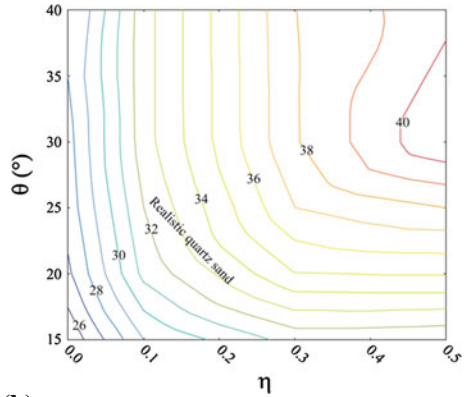
Figure 2.12b shows that on average the volumetric strain of the granular sample increases with the axial strain, which suggests that the dense granular sample would dilate during the triaxial tests. The volumetric strain tends to remain constant at the critical state. At any specific value of axial strain, the magnitude of volumetric strain increases with the inter-particle friction angle. For samples with different θ , the peak and constant volume material internal friction angles are given in Table 2.2.

To investigate the influence of grain rolling resistance on the soil strength properties, a series of triaxial tests using different values of rolling plastic moment have been conducted in this research. As shown in Fig. 2.13a, the rolling plastic

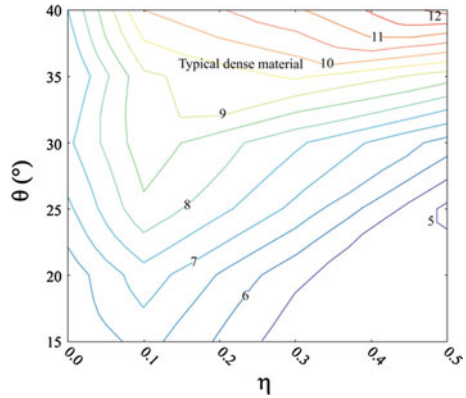
Fig. 2.11 Contours of material internal friction angles for different combinations of θ and η



(a) peak material internal friction angle (φ_{peak} ($^{\circ}$))

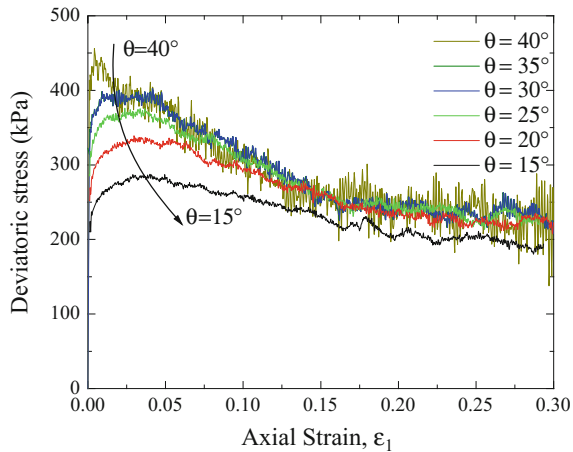


(b) constant volume material internal friction angle (φ_{cv} ($^{\circ}$))

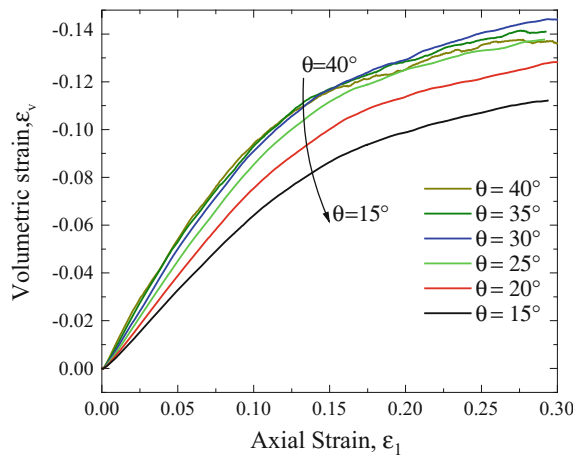


(c) $\varphi_{peak} - \varphi_{cv}$

Fig. 2.12 Results of triaxial test using different friction angles ($\beta = 1.0, \eta = 0.1$)



(a) relationship between the deviatoric stress and axial strain



(b) relationship between the volumetric strain and axial strain

Table 2.2 The peak and constant volume material internal friction angles ($\beta = 1.0, \eta = 0.1$)

θ (°)	15	20	25	30	35	40
φ_{peak} (°)	35.7	38.6	40.4	41.4	41.5	42.6
φ_{cv} (°)	29	31.3	32	32.6	32.6	32.6

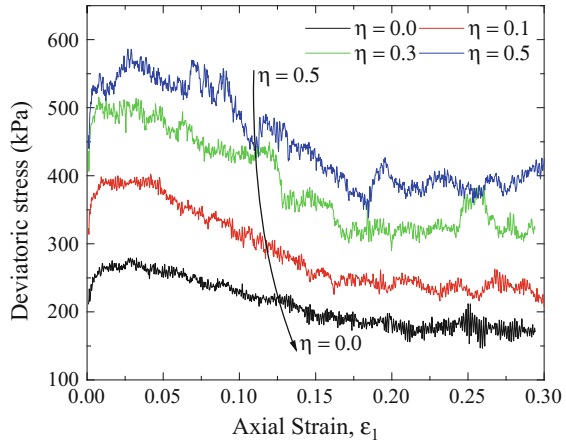
moment can influence both the peak and critical state strengths of soil significantly. On average, the magnitudes of peak and critical state strengths increase with η . Figure 2.13b shows that the volumetric strain of sand sample varies little as η increases from 0.1 to 0.5. However, for the simulation with η of 0.0 (i.e. free rolling particles), the volumetric strain is smaller than those of other simulations, indicating that the dilation of granular sample during shearing is not significant for free rolling

particles. This phenomenon is similar to the results obtained by Modenese (2013). For samples using different coefficients of rolling plastic moment, the peak and constant volume material internal friction angles are summarized in Table 2.3.

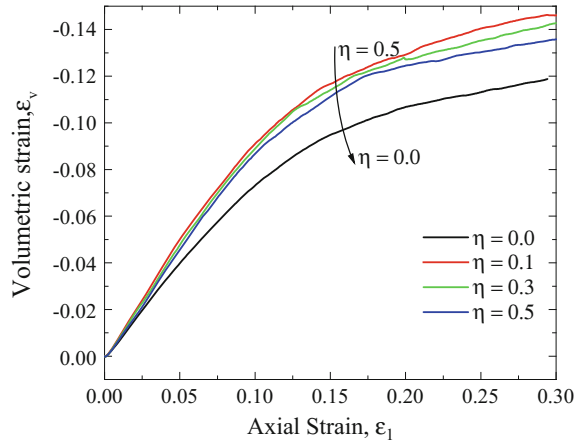
2.2.4 Material Angle of Repose

To study the depositional behaviour non-cohesive granular materials, it is useful to measure the angle of repose. This variable is defined as the steepest angle of the descent of slope relative to the horizontal plane, when grains on the slope surface are on the verge of sliding (Lowe 1976). The granular materials start to move if the

Fig. 2.13 Results of triaxial tests using different coefficients of plastic moment ($\theta = 30$, $\beta = 1.0$)



(a) relationship between the deviatoric stress and axial strain



(b) relationship between the volumetric strain and axial strain

Table 2.3 The peak and residual friction angles ($\theta = 30$, $\beta = 1.0$)

η	0	0.1	0.3	0.5
$\varphi_{\text{peak}} (^{\circ})$	35.0	41.4	45.5	47.2
$\varphi_{\text{cv}} (^{\circ})$	27.6	32.6	37.9	40.9

slope inclination angle is above the angle of repose, while it is stable if the slope angle is below the angle of repose. The typical values of angle of repose can range from 25° (for smooth spherical particles) to 40° (for rough angular particles) (Carrigy 1970; Pohlman et al. 2006). Once in motion, the grains would flow below the angle of repose, while at the end of the flow, the granular materials would deposit at the angle of repose (Hungr 1995; Walton et al. 2007; Mangeney et al. 2010). Theoretically, the angle of repose is approximately close to the macroscopic material internal friction angle (φ). This section will calibrate the angle of repose, as a verification of the material internal friction angle discussion in Sect. 2.2.3.

A simple granular column collapse model is used to study the angle of repose. As shown in Fig. 2.14a, the solid grains (i.e. dry sand used in this research) are poured into a vertically placed container to form a static sand pile. The width and height of the pile are 0.05 m and 0.05 m, respectively. After consolidation, the frontal boundary (B) is removed quickly, so that the granular materials can fall downwards under gravity and spread horizontal along the ground floor. The horizontal ground floor is covered with solid grains of the same properties as grains in the pile, so that the roughness of the ground floor can be modelled. When all the grains stop moving, the angle of repose is measured as the steepest angle of the deposit profile (Fig. 2.14b). In addition, it is also possible to observe a failure plane of the slope, which is defined as the sliding surface of the granular flow.

In order to simulate the mechanical behaviour of debris materials, the numerical model should produce the same angle of repose as that observed in laboratory experiments. As suggested by Lube et al. (2005), the angle of repose for different granular materials used in small-scale laboratory experiments ranges from 29° to 35°, as listed in Table 2.4. The grain properties of the DEM sample used in this research can approximately match that of coarse quartz sands, in which the angle of repose is close to 31°. Thus, in the numerical model, the microscopic friction angle

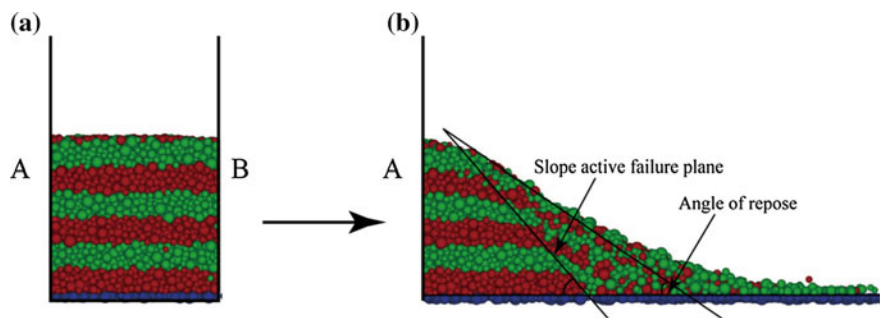


Fig. 2.14 Model configuration for testing the granular angle of repose

Table 2.4 Grain properties used in experiments (data cited from Lube et al. 2005)

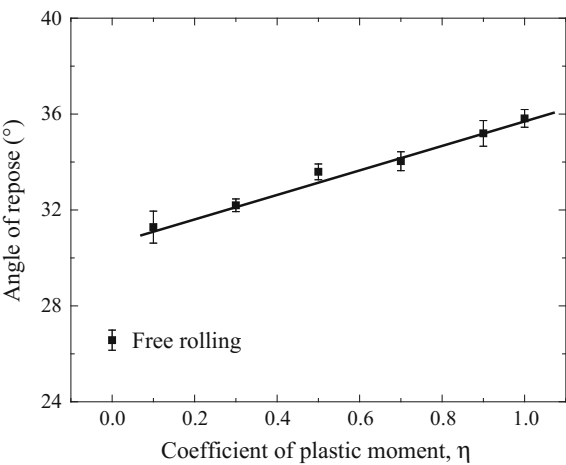
Particle	Mean density (g/cm ³)	Mean grain size (mm)	Angle of repose (°)
Fine quartz sand	2.6	0.15	29.5
Coarse quartz sand	2.6	1.5	31
Sugar	1.58	1	35
Rice	1.46	4.5	32

between grains has initially been set as 30°, while the rolling resistance parameters (of particular importance is the coefficient of plastic moment (Modenese et al. 2012)) increase gradually from the minimum value of 0.0 to the maximum value of 1.0. During this process, the rolling stiffness is assumed to change very little, as is expected not to influence the debris motion significantly.

2.2.4.1 Results

In a normal gravity field (1 g), the relationship between the macroscopic angle of repose and the coefficient of plastic moment in the microscopic rolling resistance model is shown in Fig. 2.15. It can be observed that the simulation with η being 0.0 can lead to a relatively small angle of repose, while simulations with $\eta > 0.0$ can reproduce realistic angles of repose, when compared to that of materials used in laboratory experiments. When the rolling resistance model is active, there is a sudden increase of the angle of repose. This result is in accordance with the conclusions made by Rothenburg and Bathurst (1992); Pöschel and Buchholtz (1993) and Modenese (2013) that the free rolling spherical particles have a smaller angle of repose than the spherical particles with rolling resistance.

Fig. 2.15 Angle of repose for granular materials with different rolling resistance (for each point, the error bar is achieved for two measurements at different locations on the slope surface)



According to Fig. 2.15, the numerical results obtained from the simulations using a combination of inter-particle friction angle of 30° and the coefficient of rolling plastic moment of 0.1 can lead to an angle of repose being equal to 31.3° , which is close to the value of coarse quartz grains given by Lube et al. (2005) and the constant volume material internal friction angle calibrated in Sect. 4.3.1.

2.3 Conclusions

This chapter has outlined the DEM model and the configurations of numerical model used in this research, based on which, a series of calibration tests were carried out with three main objectives: (i) to determine the time step for simulations of granular flows; (ii) to calibrate the angle of repose and material internal friction angle for the DEM model; and (iii) to give insights into the mechanical and deformational behaviour of sand under shearing. The main findings and remarks can be concluded as

- (i) A combination of microscopic friction angle of 30° and rolling plastic moment coefficient of 0.1 can produce an angle of repose of 31.3° and a material internal friction angle of 32.6° , respectively. These two parameters can qualitatively match the property of coarse quartz sands and will be used in the simulations in the following chapters.
- (ii) In the triaxial tests, different combinations of θ and η can lead to distinct values of material internal friction angle, as represented by the contour curves in this chapter. These graphs can be used as guidelines for selecting appropriate microscopic particle friction and rolling resistance parameters in the DEM model.
- (iii) The un-damped particle collision model is used in this research to determine the numerical time step used in the DEM simulations. Based on the input parameters, a DEM time step of 10^{-7} s is chosen for simulations of granular flows.

Coupled DEM-CFD Analyses of Landslide-Induced Debris
Flows

Zhao, T.

2017, XV, 220 p. 132 illus., 82 illus. in color., Hardcover

ISBN: 978-981-10-4626-1